

Supplementary materials and methods.

Cholesterol (Chol), 1,2-Dipalmitoyl-*sn*-Glycero-3-Phosphocholine (DPPC), 1,2-Dioleoyl-*sn*-Glycero-3-Phosphocholine (DOPC), Ganglioside GM1, and 1,2-Distearoyl-*sn*-Glycero-3-Phosphoethanolamine-N-[Biotinyl(Polyethylene Glycol)2000] (DSPE-Bio-PEG2000) were purchased from Avanti Polar Lipids, Inc. (Alabaster, AL). Casein, tris, and ethylenediaminetetraacetic acid (EDTA) were obtained from Fisher Scientific (Fairlawn, NJ). Fatty-acid free bovine serum albumin (BSA) was purchased from Sigma Chemical Co. (St. Louis, MO). Texas Red-1,2-dihexadecanoyl-*sn*-glycero-3-phosphoethanolamine triethylammonium salt (Texas-Red-DHPE) and Cholera toxin subunit B (CTB)-Alexa Fluor 488 (A488) were from Invitrogen (Carlsbad, CA). Streptavidin conjugated microspheres with mean diameter of ~6 μm were from Polysciences, Inc. (Warrington, PA).

Preparation of Giant Unilamellar Vesicles

Lipid solutions were prepared to contain 37 mol% DPPC, 33 mol% Chol, and 30 mol% DOPC dissolved in chloroform for a total lipid concentration of 1 mM, and additionally contained 0.3 mol% Texas-Red-DHPE, and 0.5 mol% DSPE-Bio-PEG2000. For experiments where CTB-binding was desired, 1 mol% of GM1 was added. GUVs were prepared by electroformation as described(1). Briefly, 70 μL of lipid solution was spread onto the electrically conductive sides of two ITO-coated glass slides (Delta Technologies Ltd, Stillwater, MN) at 60 $^{\circ}\text{C}$. The slides were placed under vacuum for at least 2 h, then combined with a silicone spacer and filled with 100 mM sucrose solution. The slides were connected to an AC field (2 V/mm, 5 Hz) and maintained at 60 $^{\circ}\text{C}$ for 2 h.

Preparation of micropipettes

Micropipettes were fashioned from glass capillaries (World Precision Instruments Inc., Sarasota, FL) that were stretched using a pipette puller. Pipette tips were cut using a microforge at desired inner diameters of ~3 μm . Irreversible adhesion of membrane to the pipette was prevented by incubation of pipette tips in 0.5 mg/mL BSA dissolved in 1X PBS. Pipettes were filled with 120 mM sucrose solution using a MicroFil needle (WPI, Sarasota, FL).

Tube domain growth

Tube domain growth experiments were performed using two different microscopes: a combined double micropipette / fluorescence confocal microscopy setup (Fig. 1A) which has been described before (see Ref. (2)) and a combined optical trapping / fluorescence microscopy system (Fig. 1B), which we detail below.

A sample chamber was formed from two coverslips overhanging both sides of a glass microscope slide, creating a 1 mm thick cell that was open on three sides to allow the insertion of a micropipette. The coverslips were pretreated by immersion in a solution of 2.5 mg/mL casein, 20 mM tris, and 2 mM EDTA and subsequent rinsing with deionized water. The chamber was filled with 100 μL of 125 mM sucrose, 1.5 μL of 10X PBS, 0.2 μL of microsphere dispersion, and 0.3 μL of vesicle dispersion. The chamber was mounted on an inverted microscope (IX81; Olympus, Center Valley, PA) equipped with a 60X 1.2NA water immersion objective with coverslip correction (Olympus), a Texas Red filter cube (Chroma, Rockingham, VT), and a back-illuminated electron-multiplying charge-coupled-device (EM-CCD) camera (ImagEM; Hamamatsu, Bridgewater, NJ). The microscope is further equipped with a home-built optical trapping (laser tweezer) system which uses a second, independently positioned objective (60X, 1.1NA, water immersion, long working distance; Olympus) oriented opposite the imaging objective to introduce a 1064 nm fiber optic laser into the chamber (Fig. 1B). A single micropipette was inserted into the chamber with the use of a three-dimensional motorized

micromanipulator system (Luigs & Neumann, Ratingen, Germany). Following insertion, zero pressure across the pipette tip was attained and calibrated by watching the flow of small fluorescent particles within the tip. Aspiration pressure was controlled through adjustments in the height of an attached water reservoir, and it was measured with a pressure transducer (Validyne Engineering, Los Angeles, CA). The chamber was allowed to sit for ~15 minutes such that a majority of the beads and vesicles settled to the chamber floor. Vesicles were then selected which primarily consisted of two large domains (with Lo phase fraction > 0.5); which had sufficient excess area such that aspiration at low pressure led to a projection with length greater than the pipette radius; and, which were roughly 10 to 30 μm in diameter. The aspiration pressure was increased to a low value (~10 Pa), and the Ld portion of the vesicle pulled into the pipette. The aspirated vesicle was repositioned somewhat higher in the chamber (~80 μm) to minimize interference from other vesicles and beads. The trapping objective was brought to focus on a membrane-free bead, after which the trapped bead was then positioned adjacent and coplanar to the aspirated vesicle. The Lo portion of the vesicle was moved into contact with the bead and then retracted slowly to a distance of ~10 μm , forming a tube between the bead and vesicle. This tube was initially completely within the Lo phase. The aspiration pressure was increased sharply, after which an Ld domain was observed to nucleate at the tube neck region of the vesicle. This domain grew in the direction of the bead. After domain growth over a few minutes, the pressure was further increased and a “fresh” tube region was generated by retracting the bead by 40 μm . Immediately thereafter, both the tube neck and adjacent length of tube were once again completely in the Lo phase; the previously generated Ld domain had been pulled further along the tube and was completely removed from the vesicle. A new domain nucleated at the tube neck and again grew in length, and this process could be repeated several times.

Optical trap design and calibration

A 1064 nm continuous wave fiber optic laser (IPG Photonics, Oxford, MA) with an output power of 2 W was passed through a half-wave plate (Thorlabs, Newton, NJ) and a polarizing beam splitter cube (Newport, Irvine, CA) to split the laser into a trapping component, and a second component which was redirected into a beam dump. In this manner, the relative power levels of each portion could be controlled through rotation of the half-wave plate without resorting to changing the diode laser current(3). The trapping laser was then passed through a 3.33X beam expander (Thorlabs) to overfill the back aperture of the trapping objective. In order to allow movement of a trapped bead over distances of several millimeters at constant trap stiffness, the laser was reoriented to travel parallel to the x-axis of a motorized stage (MS-2000; Applied Scientific Instrumentation, Eugene, OR). The x-axis of the motorized stage was parallel to the tube pulling direction. An IR beamsplitter was mounted on the stage to redirect the laser perpendicular to the x-axis and parallel to the optical axis of the microscope – and a long working distance, 60X, 1.1 NA water immersion microscope objective (Olympus) to focus the laser. In this fashion, the stage, beamsplitter, and trapping objective could be moved simultaneously along the axis used to pull tubules from GUVs while maintaining a constant beam power, orientation, and profile through the trapping objective, thus stabilizing the trap stiffness at all positions. Also attached to the trapping objective assembly were optics to pass optically filtered blue light from the transmitted light lamp head of the microscope onto a trapped bead, and to collect the resultant backscattered light onto a CCD camera (XC-ST30; Sony, Park Ridge, NJ). The backscatter image was thereby fixed relative to the focal point of the trapping objective. The trap was calibrated using the drag-force method, in which the motorized stage was used to drag a trapped bead through the chamber at several fixed velocities(4). During the stage

movement, hydrodynamic forces acted on the bead as $f_{drag} = 6\pi\eta rv$, where η is the viscosity of the solution, r is the bead radius, and v is the velocity at which it is moved. The bead was imaged via the backscatter light-collecting CCD mounted on the motorized stage, and its center was determined with custom image-fitting algorithms written in Matlab (The Mathworks, Natick, MA). Since the camera was fixed relative to the trapping objective, the image of the bead was displaced from its stationary position only while the stage was moving. The displacement is related to the hydrodynamic force exerted at the specified velocity by the trap stiffness as for a Hookean spring: $f_{drag} = k\Delta x$, where k is the trap stiffness and Δx is the displacement of the bead. The trap stiffness was typically 0.05 pN/nm, and was calibrated for every individual bead used. Once the stiffness was known, subsequent imaging and determination of the bead displacement allowed us to measure the net force acting on the trapped bead in real-time (~ 20 Hz). Force measurements occurred simultaneously with measurements of aspiration pressure and fluorescence imaging by the microscope-mounted EM-CCD.

Image analysis

Quantitative image analysis was achieved using HCIMAGE (Hamamatsu), IMAGEJ (National Institutes of Health, Bethesda, MD), and FLUOVIEW (Olympus).

Line tension measurements

Domain line tension for composition DOPC:Chol:DPPC; 30:33:37 was measured by means of domain boundary flicker spectroscopy, as previously described(5). Briefly, fluctuating domains of freshly prepared vesicles were imaged with an EM-CCD camera (ImagEM, Hamamatsu, Bridgewater, NJ) mounted on an inverted microscope (1X71; Olympus, Center Valley, PA) with a 60X 0.90 numerical aperture air objective (UPlanFL N, Olympus) and a Texas Red filter cube (Chroma, Rockingham, VT). Domains with centers-of-mass positions significantly deviating from the vesicle pole during the image acquisition or with radius larger than 30 % of the vesicle radius were discarded. To reduce the effect of photo-oxidation, neutral density filters and low light intensity were used. All measurements were taken at room temperature with a frame acquisition time of 15 ms and an averaged frame rate of 65 frames per second. Normal mode analysis of domain shape tracing data were processed with MATLAB algorithms to calculate averages of line tensions using first and second set of 200 frames of a fluctuating domain movie, for five different vesicles. We obtained a value of 0.16 ± 0.062 pN.

Numerical solution of shape equations

The formalism described below is adapted from a theoretical scheme developed by Juelicher and Lipowsky(6, 7). The catenoid shape was parameterized by means of a non-dimensionalized radius r and tangent to the shape ψ , as a function of arclength of the shape s , see inset of Fig. 4A (8). The arclength s was measured from the catenoid edge, and the angle ψ was measured relative to the radial coordinate axis. We solved the resulting system of first order differential equations with the boundary value problem (bvp) solver bvp4c of Matlab (The Mathworks, Inc., Natick, MA). The bvp solver requires fixed integration intervals. In order to vary the total arclength of the shape, the equations were therefore re-parameterized using the integration variable $S \in [0 \pi]$ such that $s(S=0) = s_0 = 0$ at one end of the shape, and $s(S=\pi) = s_{end}$ at the other end(7, 9). For the phase-separated tube the two phase boundaries are localized at $s_1 = s(S_1^*)$ and $s_2 = s(S_2^*)$. In the following, derivatives with respect to s are indicated by a dash, and derivatives with respect to S are indicated by a dot. The choice of $\dot{s} = (\sin S)/r$ fixes the total area of the shape to a value corresponding to the area of a sphere with unit radius(9), since

$$A = 2\pi \int_{s_0}^{s_{end}} r ds = 2\pi \int_0^\pi \sin S dS = 4\pi. \quad (S1)$$

Similarly, fixing values S_1^* and S_2^* while varying the shape ensured constant area fractions of coexisting phases. The free energy of the membrane is given, using indices i for coexisting phases(7, 10):

$$F_i = \frac{\kappa_i}{2} \int (C_1 + C_2)^2 dA + \sigma_i \int dA + p \int dV + \frac{\gamma}{2\pi} \int (r' - \cos \psi) ds - f \int dL + 2\pi Tr(s_i) \quad (S2)$$

Here, κ is the bending stiffness, C_1 and C_2 are meridional and parallel curvatures of the axially symmetric shape, and V and L are volume and length of the shape, respectively. Furthermore, σ , p , and f are Lagrange multipliers fixing area, volume, and length of the shape, respectively. T is an additional Lagrange multiplier corresponding to the line tension at a phase boundary at position s_i . The quantity γ is also a Lagrange multiplier. Its mechanical meaning is the projection of the transverse shear along a direction orthogonal to the symmetry axis(11). Geometrically it ensures the constraint $r' = \cos \psi$ (8). For axially symmetric shapes, we have $C_1 = \psi'$ and $C_2 = (\sin \psi)/r$. We furthermore have

$$dA = 2\pi r ds \quad dV = \pi r^2 \sin \psi ds \quad dL = \sin \psi ds. \quad (S3)$$

The variation of the shape free energy in terms of the variables ψ , ψ' , r , r' , and γ can be expressed in terms of a Lagrangian defined as (mechanical variables are here divided by the bending stiffness)(10)

$$\mathcal{L}_i = \frac{r}{2} \left(\psi' + \frac{\sin \psi}{r} \right)^2 + \sigma_i r + \frac{pr^2}{2} \sin \psi + \gamma (r' - \cos \psi) - \frac{f}{2\pi} \sin \psi, \quad (S4)$$

such that $F_i = 2\pi \int \mathcal{L}_i ds + 2\pi Tr(s_i)$. Therefore, for stationary shapes:

$$\frac{\delta F_i}{2\pi} = \int \left\{ \left(\frac{\partial \mathcal{L}_i}{\partial \psi} \delta \psi + \frac{\partial \mathcal{L}_i}{\partial \psi'} \delta \psi' \right) + \left(\frac{\partial \mathcal{L}_i}{\partial r} \delta r + \frac{\partial \mathcal{L}_i}{\partial r'} \delta r' \right) + \frac{\partial \mathcal{L}_i}{\partial \gamma} \delta \gamma \right\} ds + T \delta r(s_i) = 0, \quad (S5)$$

Integrating the bracketed terms in Eq. S5 by parts yields two Euler-Lagrange equations for each domain i plus two boundary conditions at each phase boundary. From the Euler-Lagrange equations one obtains three first order ordinary differential equations (DEQs) for the first domain (which is an Lo phase domain), after dividing by the bending stiffness of the Lo phase:

$$\psi' \equiv U \quad (S6)$$

$$U' = -\frac{\psi' \cos \psi}{r} + \frac{\sin \psi \cos \psi}{r^2} + \frac{pr \cos \psi}{2} + \frac{\gamma \sin \psi}{r} - \frac{f}{2\pi r} \cos \psi \quad (S7)$$

$$\gamma' = \frac{U^2}{2} - \frac{\sin^2 \psi}{2r^2} + pr \sin \psi + \sigma_1. \quad (\text{S8})$$

For the second domain, i.e. the Ld domain, which has a different bending stiffness, the equivalents to Eqs. S7 and S8 are

$$U' = -\frac{\psi' \cos \psi}{r} + \frac{\sin \psi \cos \psi}{r^2} + \frac{\varepsilon pr \cos \psi}{2} + \frac{\varepsilon \gamma \sin \psi}{r} - \frac{\varepsilon f}{2\pi r} \cos \psi \quad (\text{S9})$$

$$\gamma' = \frac{U^2}{2\varepsilon} - \frac{\sin^2 \psi}{2r^2 \varepsilon} + pr \sin \psi + \sigma_2, \quad (\text{S10})$$

where $\varepsilon = \kappa_{Lo}/\kappa_{Ld}$ is the ratio of bending stiffness values in Lo and Ld phase, respectively. For the third domain, the shape equations are essentially those of Eqs. S6 to S8. For each domain, we use the following three additional DEQs:

$$r' = \cos \psi \quad (\text{S11})$$

$$z' = -\sin \psi \quad (\text{S12})$$

$$\sigma'_i = 0. \quad (\text{S13})$$

Eq. S12 is an auxiliary DEQ that is used to find the z coordinate of a point on the shape, and Eq. S13 ensures that the lateral tension in each domain is spatially constant. The system of 18 differential equations (six for each domain) is integrated using the fixed integration variable $S \in [0, \pi]$, instead of using the arclength of the deformed shape, s . This requires that the integration intervals be expressed for each domain as function of $S \in [0, \pi]$. For the first domain, we have $S_1 = SS_1^*/\pi$, for the second domain $S_2 = S_2^* - S(S_2^* - S_1^*)/\pi$, and for the third domain we use $S_3 = \pi - S(\pi - S_2^*)/\pi$. It follows that $ds_1 = dS(S_1^*/\pi) \sin S_1/r$, $ds_2 = -dS((S_2^* - S_1^*)/\pi) \sin S_2/r$, and $ds_3 = -dS((\pi - S_2^*)/\pi) \sin S_3/r$, for first through third domain, respectively.

The system of 18 DEQs requires 18 boundary conditions. Six of these are defined at the two ends of the shape. At the catenoid edge, where we have $s = s_0 = 0$, we require

$$U(s_0) + \frac{\sin \psi(s_0)}{r(s_0)} = 0 \quad (\text{S14})$$

$$\sigma_1 - \sigma_{catenoid} = 0. \quad (\text{S15})$$

$$z(s_0) = 0 \quad (\text{S16})$$

Eq. S14 sets the mean curvature at the catenoid edge to zero (free hinge boundary condition)(12) and Eq. S15 fixes the lateral tension to a value of choice. At the tip of the tube, where $s = s_{end}$ we enforce (neglecting normal pressure difference, appropriate for a thin tube(13))

$$\frac{1}{2r(s_{end})^2} + \sigma_3 - \frac{f}{2\pi r(s_{end})} = 0 \quad (\text{S17})$$

$$\psi(s_{end}) - \pi/2 = 0 \quad (\text{S18})$$

$$\gamma(s_{end}) = 0 \quad (\text{S19})$$

Eqs. S17-S19 are a consequence of assuming perfect cylinder geometry at the tube tip. Eq. S17 is the mechanical force balance (mechanical quantities are divided by the bending stiffness), Eq. S18 orients the tangent angle appropriately for an axially symmetric cylinder, and Eq. S19 follows from the fact that the transverse shear projected into a direction orthogonal to the symmetry axis must be zero.

The Hamiltonian of the shape, $H_i = -\mathcal{L}_i + \psi' \partial \mathcal{L}_i / \partial \psi' + r' \partial \mathcal{L}_i / \partial r'$, reads:

$$H_i = \frac{r}{2} \left(U^2 - \frac{\sin^2 \psi}{r^2} \right) - \frac{pr^2}{2} \sin \psi - \sigma_i r + \gamma \cos \psi + \frac{f \sin \psi}{2\pi} \quad (\text{S20})$$

Accounting for cylinder geometry at the membrane edge, neglecting the pressure term (appropriate for a thin cylinder), and inserting Eqs. S17 and S18 shows that $H = 0$ at the tube tip. The Hamiltonian is furthermore conserved, and therefore $H = 0$ all along the shape.

Additional boundary conditions connect the shape at the two phase boundaries, and we require six boundary conditions at each phase boundary. Three of these ensure the continuity of the shape, i.e. angle, radius, and the coordinate z have to have the same values immediately before and after each phase boundary. The remaining three phase boundary conditions are mechanical jump conditions. They are obtained from the two boundary terms of the Euler-Lagrange equations and they read (indices indicate value immediately before and after the respective phase boundary):

$$\gamma_1 - \gamma_2 + T = 0, \quad \gamma_2 - \gamma_3 + T = 0 \quad (\text{S21})$$

as well as

$$U_1 + \left(\frac{\sin \psi}{r} \right) - \frac{1}{\varepsilon} \left(U_2 + \left(\frac{\sin \psi}{r} \right) \right) - \zeta \frac{\sin \psi}{r} = 0 \quad (\text{S22})$$

at the first phase boundary, whereas

$$\frac{1}{\varepsilon} \left(U_2 + \left(\frac{\sin \psi}{r} \right) \right) - \left(U_3 + \left(\frac{\sin \psi}{r} \right) \right) + \zeta \frac{\sin \psi}{r} = 0 \quad (\text{S23})$$

at the second phase boundary. Here $\zeta = (\kappa_G^{Ld} - \kappa_G^{Lo}) / \kappa^{Lo}$ is the Gaussian bending stiffness difference between Lo and Ld phase, made non-dimensional by dividing with the Lo phase mean curvature stiffness(7, 14). Eq. S21 means that the jump across the phase boundary of transverse shear projected along the parallels is equal to line tension. Eqs. S22 and S23 express the fact that the bending moments have to be continuous in passing the phase boundaries. The remaining set of boundary conditions is obtained from the requirement that the Hamiltonian, H , is continuous across the phase boundaries. This leads to

$$\left(\frac{U_1^2}{2} - \frac{\sin^2 \psi}{2r^2} - \sigma_1 \right) - \left(\frac{U_2^2}{2\varepsilon} - \frac{\sin^2 \psi}{2\varepsilon r^2} - \sigma_2 \right) - \frac{T}{r} \cos \psi = 0 \quad (\text{S24})$$

$$\left(\frac{U_2^2}{2\varepsilon} - \frac{\sin^2 \psi}{2\varepsilon r^2} - \sigma_2 \right) - \left(\frac{U_3^2}{2} - \frac{\sin^2 \psi}{2r^2} - \sigma_3 \right) - \frac{T}{r} \cos \psi = 0 \quad (\text{S25})$$

for the first and second phase boundary, respectively. Eqs. S24 and S25 relate the jumps in lateral tension across the phase boundary to the jumps in curvature.

Since pressure p and Gaussian bending stiffness difference ζ had minute effects on our shape series these parameters were set to zero for the shapes shown in Fig. 4 and Fig. S7.

In variations of the code, the total length of the tube is specified via an additional boundary condition. This allows determining the pulling force, f , as an eigenvalue.

Derivation of analytical transport model.

The diffusion equation for mass transport in the Ld phase tube is $D_{\alpha\beta}^{Ld} \nabla^2 \bar{\mu} = \partial \bar{\mu} / \partial t$, where $D_{\alpha\beta}^{Ld}$ is a binary inter-diffusion coefficient in the Ld phase. At steady state this relation simplifies to a Laplace equation: $\nabla^2 \bar{\mu} = 0$ (15). This steady state relation is integrated along a local spatial coordinate Z of the Ld domain (see Fig. 3), using two chemical equilibrium boundary conditions (at each end of the Ld phase tube). At the tube neck, $\bar{\mu}^{Ld} \Big|_{Z=0} = \bar{\mu}_{eq}^{Lo}$, where $\bar{\mu}_{eq}$ is the value of $\bar{\mu}$ in the flat reservoir (i.e. within the vesicle where $\bar{\mu} = \bar{\mu}(\phi_0, C_{ves} = 0)$ where C_i is the curvature in membrane region i and ϕ_0 indicates the composition (mole fraction) of the vesicle reservoir; see Fig. 3C). It is thus assumed that the value of $\bar{\mu}$ at the tube neck with curvature C_n is equal to the value in the flat reservoir(2). The second boundary condition is $\bar{\mu}^{Ld} \Big|_{Z=Z_0} = \bar{\mu}^{Lo}(\phi_0, C_t)$, where C_t is the curvature at the inner tube phase boundary (Fig. 3A). Here, composition is fixed at ϕ_0 , because we assume that the phase transition occurs at the composition defined by the binodal line of the phase diagram, see Fig. 3. This simplifying assumption implies that the Ld / Lo phase diagram is not modified by membrane curvature (see the main text for further discussion of that aspect). After integration, $\bar{\mu}(Z) = \delta \bar{\mu} \Big|_{Z_0} \cdot Z / Z_0 + \bar{\mu}_{eq}$ ($0 < Z < Z_0$), where

$\delta\bar{\mu}|_{z=Z_0} = \bar{\mu}(\phi_0, C_i) - \bar{\mu}_{eq}$, and Z_0 is the position of the phase boundary. The domain boundary velocity $v = dZ_0/dt$ is related to mass transport via the continuity relation $v\rho\Delta\phi_\varepsilon = M^{Ld}\nabla\bar{\mu}$ (15), where ρ is an area density (which for simplicity we assume to be equal in all phases), M is a mobility (an Onsager transport coefficient) in the Ld phase, and we use $\Delta\phi_\varepsilon = \phi_{Lo}R_{Lo}/R_{Ld} - \phi_{Ld}$; $\phi_{Lo} - \phi_{Ld}$ is the width of the miscibility gap (Fig. 3), and R_i is the tube radius of phase i . Note that the ratio of tube radii is related to bending stiffnesses through $R_{Lo}/R_{Ld} = \kappa_{Lo}/\kappa_{Ld} \equiv \varepsilon$; the bending stiffness ratio ε is a material property of a phase-separated tube and does not depend on curvature. We evaluate the quantity $\delta\bar{\mu}$ from a Taylor expansion(2), considering absence of an intrinsic membrane curvature preference (i.e. spontaneous curvature, causing the first order term in an expansion in curvature to disappear(2)):

$$\delta\bar{\mu}|_{z_0} = \frac{1}{2} \left(\frac{\partial^2 \bar{\mu}}{\partial C^2} \right)_0 C_i^2 = \frac{1}{2\rho} \left(\frac{\partial \kappa}{\partial \phi_\alpha} \right)_0 C_i^2, \quad (\text{S26})$$

where the index “0” of the partial differentials indicates evaluation of the partial derivatives for the flat state of the membrane(2). The domain growth in our problem therefore is assumed to be caused by a thermodynamic driving force to lipid sorting due to the composition dependence of the bending stiffness in Eq. S26 (2). Assuming the composition variation along the Ld phase tube to be small, and accordingly the curvature change along the Ld phase tube to be small, we have an approximately constant lateral (mean-) tension σ_{Ld} in the Ld phase domain of the tube: $\sigma_{Ld} = \kappa_0^{Ld} C^2 / 2$. Integration of the continuity equation mentioned above (assuming a time-independent curvature C_i at the inner tube phase boundary to approximately be equivalent to the inverse Ld tube radius C) leads to Eq. 1 of the main text.

We note that the simplifying binary description used here to reduce analytical complexity eliminates a variety of phenomena such as reverse osmosis, inverse osmosis, and blocked osmosis, which are common in ternary mixtures(16). Because the Onsager reciprocity relations become relevant only for mixtures with three or more components(16), any of the above mentioned phenomena are absent in binary mixtures.

Supplementary figure captions.

Figure S1. Domain growth dynamics are independent of total tube length and domain number order. *A)* Domain length over time for five domains grown consecutively on the same vesicle, similar to method used to obtain data in Fig. 2B but without changing aspiration pressure (membrane tension) between domains: pressure was held constant at 35 Pa (membrane tension of 0.04 mN/m). All five domains are observed to grow at the same rate regardless of nucleation order and total tube length. Solid line is a linear fit to the aggregate of all five domains. The initial length of Lo phase available for each new Ld domain to invade was kept constant at 30 μm (as depicted in S1 A *ii*). *B)* Force decays observed for three sequential domains generated at the same aspiration pressure of 22 Pa ($\sigma_{res} = 0.06$ mN/m). Decays are nearly identical in shape. *C)* Change in (secondary) domain lengths of the first four domains shown in panel *A)* immediately after being pulled entirely into the tube and far from the vesicle neck. The domain lengths increase sharply as a result of a decrease in domain radius immediately after tube elongation; they slowly decrease over time with increases in domain radius as the tube

membrane tension drops due to the nucleation and growth of a new primary domain. Times $t = 0$ for each consecutive secondary domain are defined as the times of nucleation of each following primary domain.

Figure S2. Homogeneous vesicles show rapid mechanical equilibration after tube length and aspiration pressure changes. *A)* Force response (filled circles) of a homogeneous single-phase aspirated vesicle with a tube that was quickly elongated by 30 μm at velocity of 31.5 $\mu\text{m}/\text{sec}$. The time-dependent velocity of the trap center is shown as a gray line. Tube force relaxes near to the initial value within two seconds after lateral displacement of the pulling bead was stopped. The vesicle was held at an aspiration pressure of 91 Pa (membrane tension of 0.11 mN/m). Vesicle had a nominal composition of Lo3 as listed in Table S1 and Fig. S4. Equivalent time dependence was observed for Ld phase membranes (compositions listed in Table S1), as well as pure POPC vesicles. *B)* Force response (black line) of the same vesicle and tube as in panel *A)* to rapid changes in aspiration pressure (gray line). Tube force equilibrates after membrane tension changes within < 100 ms for homogeneous vesicles. Similar behavior was observed for homogeneous Ld phase and pure POPC vesicles.

Figure S3. Curvature-induced domain nucleation and growth is distinct from diffusion of pre-existing microdomains. *A)* Fluorescence image *i* shows a dimly fluorescent tube that is entirely in the Lo phase. The aspiration pressure was 16 Pa ($\sigma_{res} = 0.027$ mN/m). The portion of the vesicle shown on the left shows a small micron-sized Ld phase domain (bright line) amid a majority Lo phase. The pulling bead is illustrated with a white dashed circle on the right. The microdomain showed diffusive mobility on the vesicle, but on approaching the neck region is attracted by the neck, as seen in image *ii*. Tube phase boundary position is indicated by white arrows. In *iii-v*, the microdomain continues to invade the tube, likely by curvature-induced domain area growth, reaching a length of 5 μm by image *v*. *B)* Pulling force immediately before and after a microdomain was locked at the tube neck. The constant force leading up to image *i* is evidence of a constant tube composition. At the moment of contact of the Ld microdomain with the tube neck, the force drops within < 1 s. Further invasion of the Lo phase by means of the growing domain locked at the neck did not measurably alter the tube force, in contrast to domain growth following nucleation at the tube neck (see Fig. 2). *C)* Similar force drops are observed for two additional vesicles in which a small Ld domain became trapped at the tube neck. Tube force here is normalized relative to the initial tube force for each vesicle, with force drops ranging between 37% and 49%. Force drops are observed to occur on similar (fast) time scales compared to slow (several minutes) force decay during domain nucleation and growth.

Figure S4. *A)* Phase diagram for ternary mixtures of DOPC, DPPC, and cholesterol showing part of the binodal line indicating the region of Lo-Ld phase coexistence(17). Ten compositions leading to homogeneous vesicles of either Lo (dark gray circles) or Ld phase (light gray circles) are indicated; these compositions are numbered and refer to compositions listed in Table S1. The nominal composition of the phase-separated mixture used in domain growth experiments is shown by the open circle. *B)* Equilibrium tube force as a function of the square-root of membrane tension for homogenous Lo (black) and Ld (gray) phase vesicles, the slopes of which are proportional to the bending stiffness of each composition; the Lo phase vesicle corresponds to composition Lo2 and has a bending stiffness of $3.0 \cdot 10^{-19}$ J, while the Ld phase vesicle corresponds to composition Ld3 and has a bending stiffness of $0.6 \cdot 10^{-19}$ J (see Table

S1). Linearity of force response indicates minimal curvature dependence of tube composition over curvature range explored(18, 19).

Figure S5. Apparent bending stiffness decays during domain growth. *A)* An aspirated phase-separated vesicle with tube maintains a constant force (gray line) prior to domain nucleation for times between -100 and zero seconds; see image *i* in panel *B*). Force begins to decrease when a domain nucleates (defining time zero) and grows in length, as evidenced in images *ii-iv*. The apparent bending stiffness (black line) over time is calculated from the pulling force and the (fixed) reservoir tension. After 700 seconds of domain growth at a constant reservoir lateral tension ($\sigma_{res} = 0.08$ mN/m), the apparent bending stiffness had decreased by a factor of 2.7. *B)* Fluorescence images showing the Lo phase of the aspirated vesicle on the left attached to the bead on the right with a tube. The 8 μm tube was initially entirely in the Lo phase (image *i*) and was dimly fluorescent. By image *ii*, a 4.2 μm domain was visible. This domain continued to grow in length towards the end of the tube as shown in images *iii* and *iv*.

Figure S6. Areas of intra-tube (secondary) domains are not affected by curvature. A domain which was pulled entirely into the tube was modulated in radius and, therefore, length by changing the reservoir tension. Slope of linear fit (thick line) is proportional to domain area, and the fit extrapolates to near-zero for vanishing lateral tension, i.e. zero curvature and infinite radius. The constant slope and zero intercept suggest constant domain area (and bending stiffness) while changing curvature.

Figure S7. Geometric and mechanical domain growth data obtained from computational shape series are similar to experimental data. Total tube length was fixed at 10 μm for all calculated shapes. *A)* Domain length as a function of time for six different membrane tensions; legend in panel *B)* applies to panels *A-D*). Time axes were obtained in an iterative fashion from analytical irreversible thermodynamics model, considering leading-edge domain boundary curvature and the total domain length obtained from shapes such as displayed in Fig. 4. The parameter A (necessary to calculate the time axis, see the main text) was chosen to be $6.67 \cdot 10^{-4} \mu\text{m}^4/\text{s}$, in order to approximate experimental time axes (Fig 2). Calculations assume bending stiffnesses for Lo and Ld phases of 364 pN·nm and 81 pN·nm, respectively, corresponding to experimentally measured values. Line tension assumed here is 0.16 pN, as measured in phase-separated vesicles with the same composition as used for domain growth experiments. Gaussian bending stiffness difference is assumed to be zero. *B)* Domain length as a function of the square-root of time; roughly linear relationships are observed (at small observation times). *C)* Time dependence of tube force. *D)* Calculated tube force shows a linear dependence on domain length, regardless of applied membrane tension, in agreement with experiments (compare to Fig. 2D).

Figure S8. Exact values of line tensions have small effects on calculated shapes. All tube shapes were calculated assuming a total tube length of 10 μm , lateral tension was 0.020 mN/m, and the parameter A (necessary to calculate a time axis, see Eq. 1 of the main text) was chosen to be $6.67 \cdot 10^{-4} \mu\text{m}^4/\text{s}$. *A)* Domain length versus time for three different line tensions: vanishing (0 pN), experimentally measured (0.16 pN), and large (1pN). *B)* Tube force versus time, conditions identical to *A)*. *C)* Tube force versus domain length. Remarkably, force/domain length relation is essentially identical before the force plateau, but differs for longer domain lengths. The force decay is larger in the presence of line tension, because line tension contributes an additional

lateral tension jump(7, 14). D) Effect of line tension on location of vesicle/tether phase boundary. Magnified view of tube neck is taken from shapes with equivalent domain lengths of $6.8 \mu\text{m}$, close to the force plateau region. Ld phase: gray lines, Lo phase: black. Large line tension is observed to pin the vesicle/tube phase boundary at the tether neck.

Figure S9. Curvature-induced domains show parabolic growth and characteristic pulling force decay, vesicle II. *A)* Four domains were sequentially nucleated at the tube neck of a single vesicle (additional examples in Figs. 2 and S10) through step-wise total tube length extension followed by domain growth at constant total tube length (and reservoir tension) as shown in schematic i). Domain length as a function of time relative to the first moment of detectable fluorescence heterogeneity at the tube neck (ii). Closed circles, open circles, closed triangles, and open triangles: domains grown at pressures of $23 \pm 0.5 \text{ Pa}$, 30 Pa , 38 Pa , and 47 Pa , respectively, corresponding to the lateral tensions in panel *D)*. *B)* Same data as in panel *A)* plotted versus \sqrt{t} . Linear fits are shown as solid lines. *C)* Double logarithmic plot of the slopes of the linear fits in panel *B)* as a function of membrane tension for 6 different vesicles and 26 vesicle tensions. Slope of a linear fit yields 1.34 ± 0.12 . *D)* Tube force is observed to decrease after domain nucleation and concomitant to growth. Black curve corresponds to the first domain generated (closed circles in panels *A)*, *B)*, and *E)*); lighter gray curves correspond to domains grown sequentially at increasing aspiration pressures as in *A)*. *E)* Tube force as a function of domain length; symbols as in panel *B)*. Solid lines are linear fits for domain lengths up to $10 \mu\text{m}$.

Figure S10. Curvature-induced domains show parabolic growth and characteristic pulling force decay, vesicle II. *A)* Three domains were sequentially nucleated at the tube neck of a single vesicle (additional examples in Figs. 2 and S9) through step-wise total tube length extension followed by domain growth at constant total tube length (and reservoir tension) as shown in schematic i). Domain length as a function of time relative to the first moment of detectable fluorescence heterogeneity at the tube neck (ii). Closed circles, open circles, and closed triangles: domains grown at pressures of $11 \pm 0.5 \text{ Pa}$, 25 Pa , and 41 Pa , respectively, corresponding to the lateral tensions in panel *D)*. *B)* Same data as in panel *A)* plotted versus \sqrt{t} . Linear fits are shown as solid lines. *C)* Double logarithmic plot of the slopes of the linear fits in panel *B)* as a function of membrane tension for 6 different vesicles and 26 vesicle tensions. Slope of a linear fit yields 0.83 ± 0.08 . *D)* Tube force is observed to decrease after domain nucleation and concomitant to growth. Black curve corresponds to the first domain generated [closed circles in panels *A)*, *B)*, and *E)*]; lighter gray curves correspond to domains grown sequentially at increasing aspiration pressures as in *A)*. *E)* Tube force as a function of domain length; symbols as in panel *B)*. Solid lines are linear fits for domain lengths up to $10 \mu\text{m}$.

Figure S11. Total tube volume from calculated shapes is predicted to increase as domain growth occurs, despite the narrower radius of the invading Ld phase relative to the Lo phase (as mandated by the difference in bending stiffnesses). Calculation shown is for total tube length of $10 \mu\text{m}$. Domain growth is accompanied by significant decreases in lateral tension of both phases in the tube as the Ld domain lateral tension approaches that of the fixed reservoir tension; this second effect plays a larger role than the first and results in a net increase in tube volume during domain growth up until the force plateau region is reached. Percent increase is relative to a tube prior to domain nucleation, and is here shown for the example case of a reservoir tension of 0.020 mN/m ; other reservoir tensions considered showed nearly identical relative increases in

tube volume. Because the tube volume increase depends on the total length of the tube, any friction effects due to water transport among tube and vesicle must also depend on the total tube length. We found no evidence for total tube length dependence on domain growth kinetics (Figs 2F and S1, and therefore rule out significant contribution from hydrodynamic friction to the observed tube growth (and force decay) dynamics. Instead, mass transfer resistance contributed by lipid diffusion, as expressed in Eq. 1 of the main text, appears to govern our experimentally observed time dependence.

Supplementary table captions.

Table S1. Compositions of homogeneous vesicles of the Lo or Ld phase as depicted in the phase diagram of Fig. S4, and corresponding bending stiffness results. Bending stiffness of a homogeneous vesicle is given by $\kappa = f^2 / 8\pi^2\sigma$, where κ is the bending stiffness, f is the tube force, and σ is the membrane tension. The bending stiffness of an individual vesicle was determined from the slope of a plot of measured tube force as a function of the square-root of membrane tension. Note that these slopes were observed to be independent of curvature (as shown in Fig S4B), consistent with a composition regime far from the consolute point(19). Final values shown are the average of three to four tubes pulled from each of five different vesicles for a given composition; the exact number N of measurements for each average is given in parentheses. Uncertainties represent standard deviations and were dominated by inter-vesicle variability. Since no clear trend was present among the compositional variations, the bending stiffnesses of the Lo and Ld phase in a phase-separated vesicle were estimated – using the averages of the 5 compositions – to be 3.64 and $0.81 \cdot 10^{-19}$ J, respectively.

Table S2. The slopes of linear fits such as in Fig 2B are squared to yield the diffusion coefficient AC^2 . The diffusion coefficients depend on curvature and, therefore, the vesicle membrane tension, and this dependence is here demonstrated for measurements within six different vesicles at varying membrane tensions. Vesicles A, B, and C correspond to the data shown in Figs 2A-D, S9, and S10, respectively. This data is also shown collectively in Fig 2E.

Supplementary movie captions.

Movie 1. Ld phase tubes can be pulled out of Lo phase domain of a vesicle at low pulling speeds. A tube was pulled slowly from the ordered phase of the vesicle at an average pulling speed of about $0.04 \mu\text{m/s}$. A continuous Ld tube was generated from the Lo phase of the vesicle.

Movie 2. Lo phase tubes are pulled out of Lo phase domain of a vesicle at high pulling speeds. A tube was pulled at high speed of $1.5 \mu\text{m/s}$, resulting in an Lo tube. Reservoir membrane tension for movies 1 and 2 was $\sigma = 3.5 \cdot 10^{-5}$ N/m.

Supplementary references.

1. Mathivet L, Cribier S, & Devaux PF (1996) Shape Change and Physical Properties of Giant Phospholipid Vesicles Prepared in the Presence of an AC Electric Field. *Biophysical Journal* 70:1112 - 1121.
2. Tian A & Baumgart T (2009) Sorting of lipids and proteins in membrane curvature gradients. *Biophysical Journal* 96:2676 - 2688.
3. Lee WM, Reece PJ, Marchington RF, Metzger NK, & Dholakia K (2007) Construction and calibration of an optical trap on a fluorescence optical microscope. *Nature Protocols* 2(12):3226-3238.
4. Svoboda K & Block SM (1994) Biological Applications of Optical Forces. *Annual Review of Biophysics and Biomolecular Structure* 23:247-285.
5. Esposito C, *et al.* (2007) Flicker spectroscopy of thermal lipid bilayer domain boundary fluctuations. *Biophysical Journal* 93(9):3169-3181.
6. Julicher F. & Lipowsky R. (1993) Domain-Induced Budding of Vesicles. *Physical Review Letters* 70(19):2964 - 2967.
7. Julicher F. & Lipowsky R. (1996) Shape transformations of vesicles with intramembrane domains. *Physical Review E* 53(3):2670 - 2683.
8. Seifert U., Berndl K., & Lipowsky R. (1991) Shape Transformation of Vesicles: Phase Diagram for Spontaneous-curvature and bilayer-coupling models. *Physical Review A* 44(2):1182 - 1202.
9. Jenkins JT (1976) Static Equilibrium Configurations of a Model Red Blood Cell. *J. Math. Biology* 4:149 - 169.
10. Bozic B, Svetina S, & Zeks B (1997) Theoretical analysis of the formation of membrane microtubes on axially strained vesicles. *Physical Review E* 55(5):5834-5842.
11. Umeda T, Nakajima H, & Hotani H (1998) Theoretical analysis of shape transformations of liposomes caused by microtubule assembly. *Journal of the Physical Society of Japan* 67(2):682-688.
12. Allain JM, Storm C, Roux A, Amar MB, & Joanny JF (2004) Fission of a multiphase membrane tube. *Physical Review Letters* 93(15):1581041 - 1581044.
13. Evans E. & Yeung A. (1994) Hidden Dynamics in Rapid Changes of Bilayer Shape. *Chemistry and Physics of Lipids* 73:39 - 56.
14. Baumgart T, Das S, Webb WW, & Jenkins JT (2005) Membrane elasticity in giant vesicles with fluid phase coexistence. *Biophysical Journal* 89(2):1067-1080.
15. Langer JS (1980) Instabilities and pattern formation in crystal growth. *Reviews of Modern Physics* 52(1):1 - 28.
16. Taylor R & Krishna R (1993) *Multicomponent mass transfer* (John Wiley & Sons, Inc, New York).
17. Veatch SL & Keller SL (2003) Separation of Liquid Phases in Giant Vesicles of Ternary Mixtures of Phospholipids and Cholesterol. *Biophysical Journal* 85(5):3074 - 3083.
18. Tian A, Capraro BR, Esposito C, & Baumgart T (2009) Bending Stiffness Depends on Curvature of Ternary Lipid Mixture Tubular Membranes. *Biophysical Journal* 97(6):1636-1646.
19. Sorre B, *et al.* (2009) Curvature-driven lipid sorting needs proximity to a demixing point and is aided by proteins. *Proceedings of the National Academy of Sciences of the United States of America* 106(14):5622-5626.

Fig S1

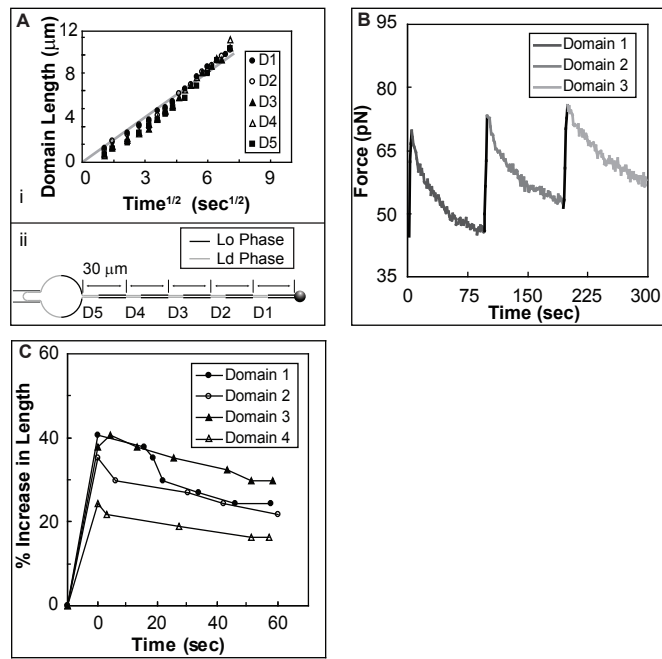


Fig S2

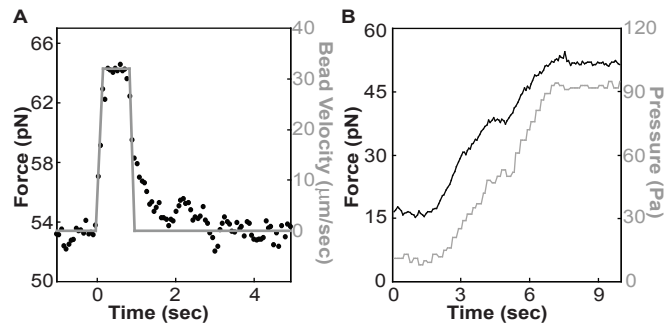


Fig S3

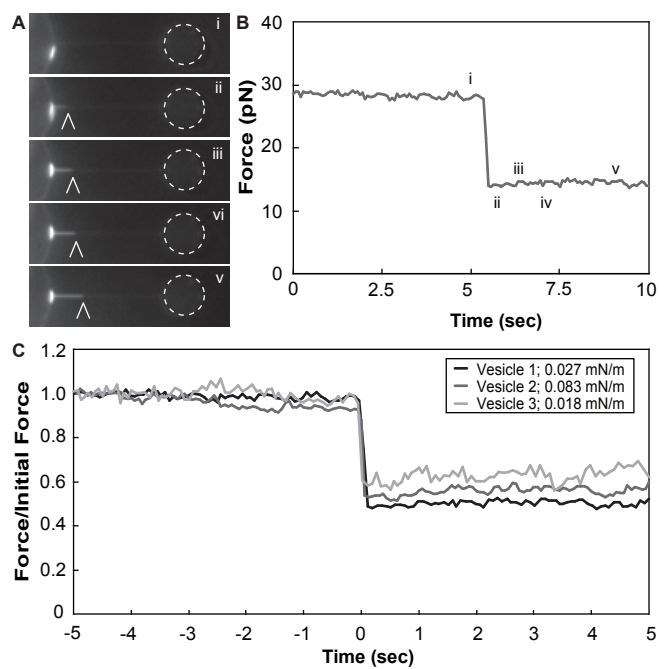


Fig S4

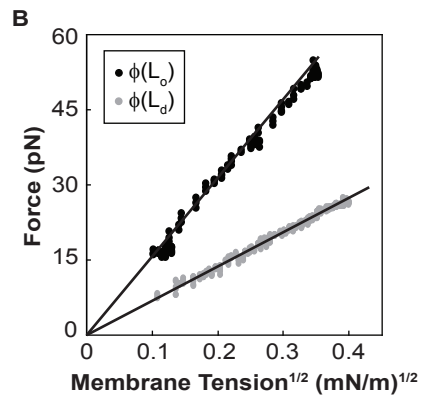
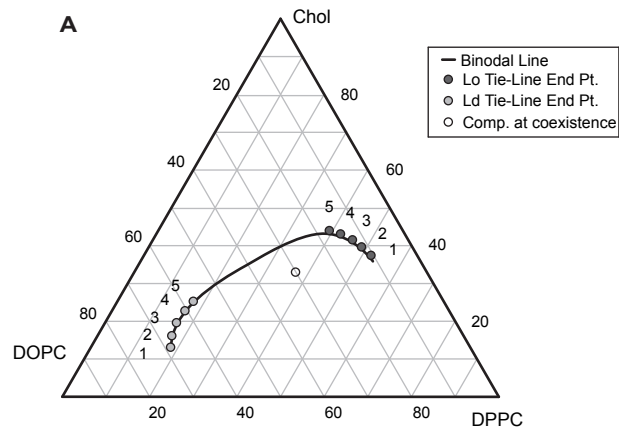


Fig S5

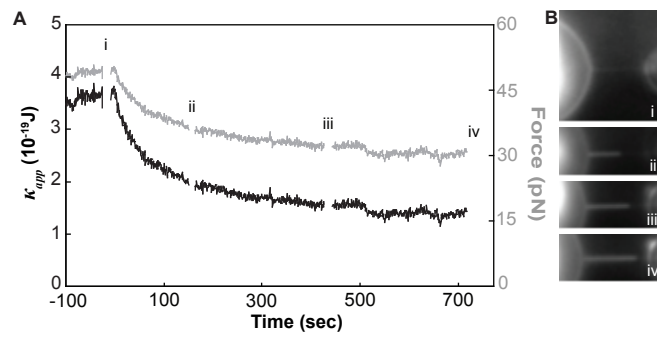


Fig S6

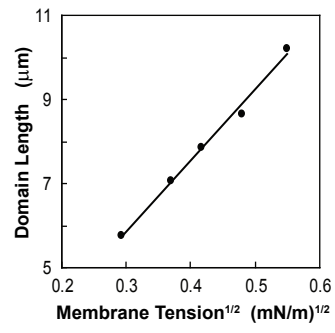


Fig S7

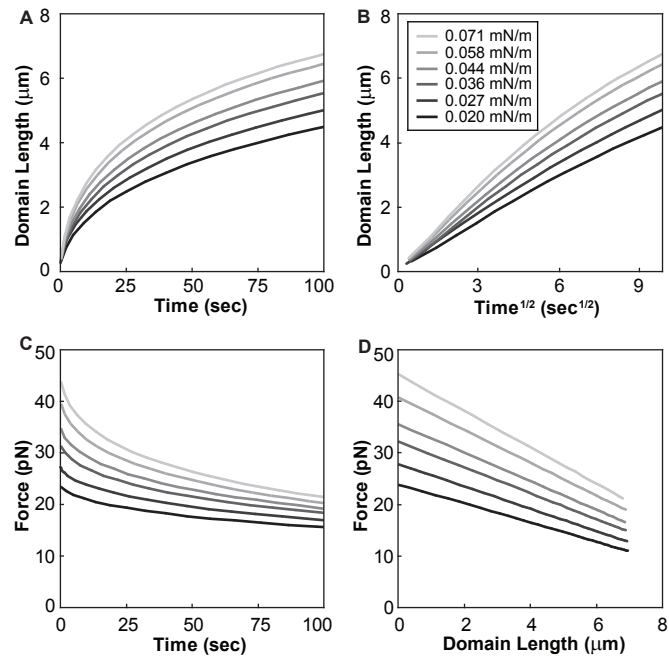


Fig S8

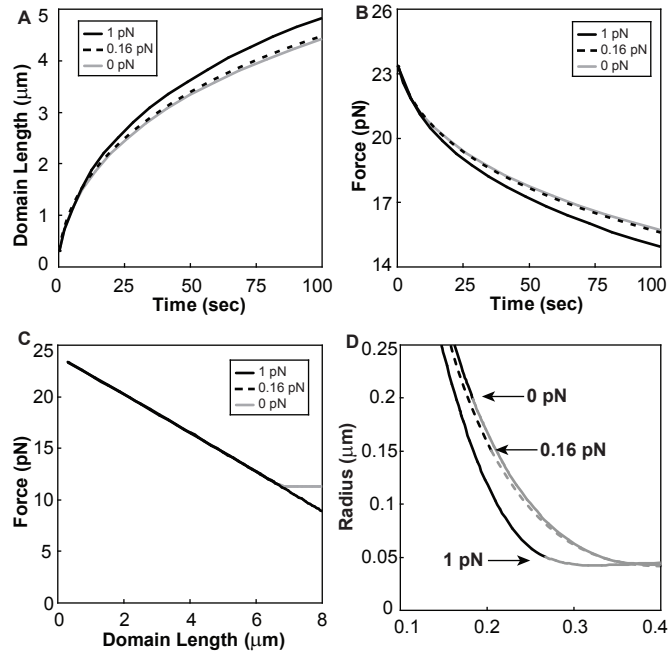


Fig S9

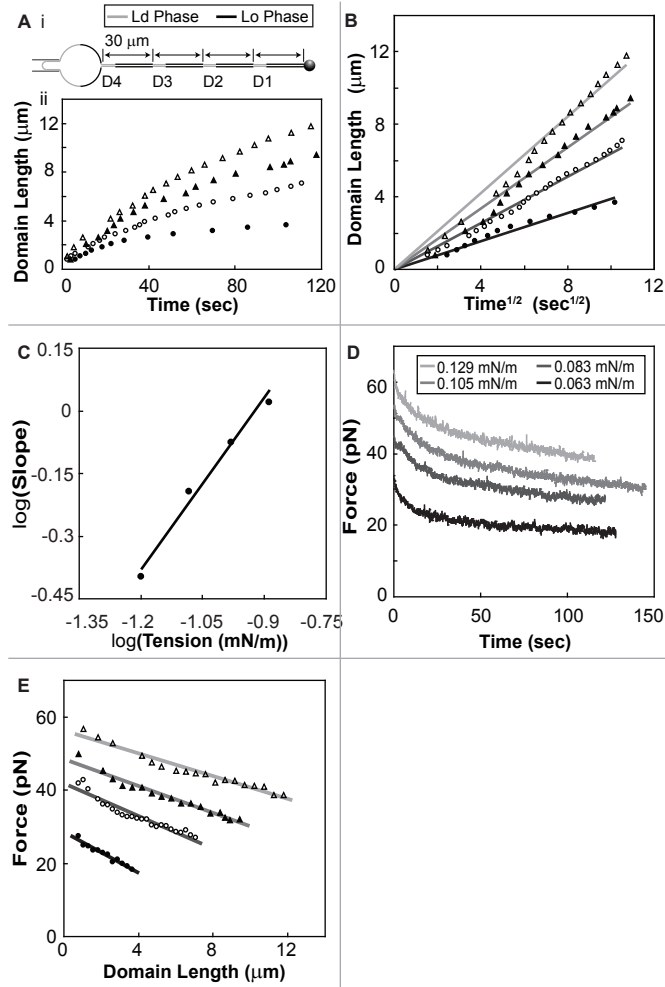


Fig S10

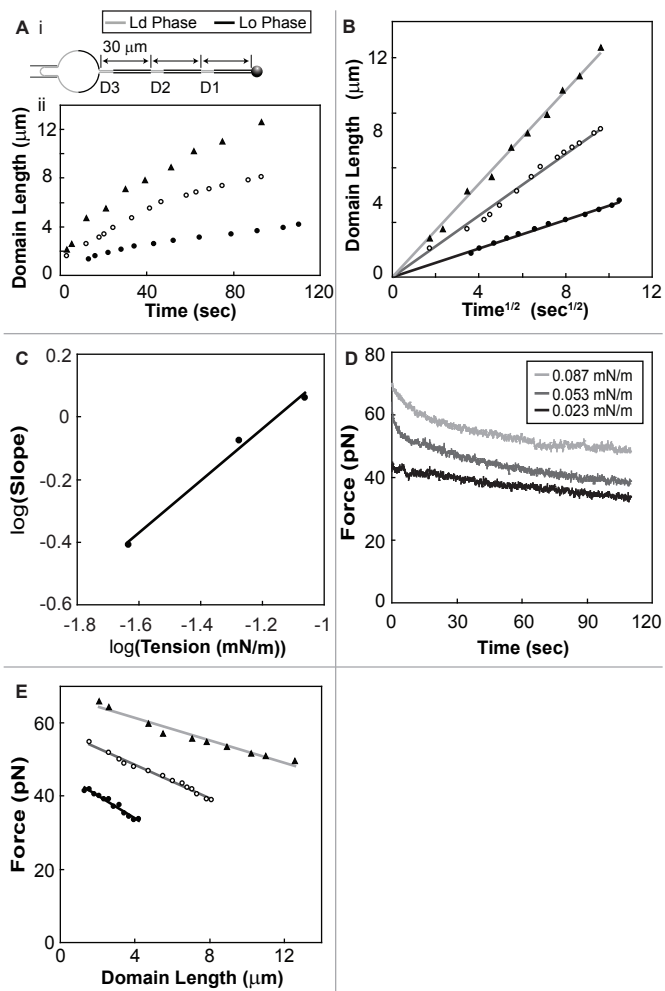


Fig S11

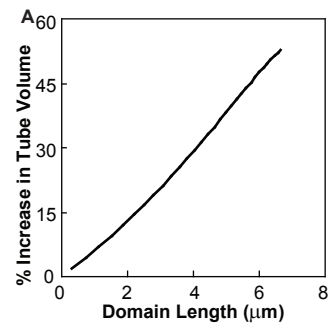


Table S1. Measured bending stiffnesses of homogenous vesicles in the Lo and Ld phase.

Composition	DPPC	DOPC	Chol	κ (10^{-19} J)
Lo1	52%	11%	37%	4.2 ± 0.9 ($N=17$)
Lo2	48%	13%	39%	3.2 ± 0.7 ($N=17$)
Lo3	46%	12%	42%	4.2 ± 0.6 ($N=24$)
Lo4	42%	15%	43%	4.0 ± 0.7 ($N=18$)
Lo5	39%	17%	44%	2.7 ± 0.2 ($N=19$)
Ld1	18%	68%	14%	0.82 ± 0.06 ($N=16$)
Ld2	17%	66%	17%	0.87 ± 0.08 ($N=18$)
Ld3	16%	64%	20%	0.73 ± 0.09 ($N=15$)
Ld4	17%	60%	23%	0.71 ± 0.06 ($N=16$)
Ld5	17%	57%	26%	0.94 ± 0.12 ($N=17$)

Table S2. Experimentally measured diffusion coefficients depend on membrane tension.

Vesicle	Membrane Tension (mN/m)	Diffusion Coefficient ($\mu\text{m}^2/\text{s}$)
A	0.020±0.003	0.18±0.01
A	0.027±0.005	0.30±0.01
A	0.036±0.006	0.38±0.02
A	0.044±0.008	0.59±0.02
A	0.058±0.010	0.76±0.02
A	0.071±0.012	1.42±0.03
B	0.063±0.011	0.16±0.01
B	0.083±0.014	0.41±0.02
B	0.11±0.02	0.71±0.02
B	0.13±0.02	1.10±0.02
C	0.023±0.004	0.15±0.01
C	0.053±0.009	0.71±0.02
C	0.09±0.02	1.32±0.03
D	0.054±0.009	0.10±0.01
D	0.072±0.012	0.19±0.01
D	0.09±0.02	0.26±0.01
D	0.10±0.02	0.48±0.02
D	0.12±0.02	0.71±0.02
D	0.15±0.03	1.30±0.03
E	0.056±0.009	0.26±0.01
E	0.075±0.013	0.95±0.02

E	0.10 ± 0.02	1.72 ± 0.03
E	0.11 ± 0.02	2.95 ± 0.06
F	0.045 ± 0.008	0.19 ± 0.01
F	0.13 ± 0.02	3.35 ± 0.07
F	0.18 ± 0.03	6.45 ± 0.13
F	0.21 ± 0.04	9.9 ± 0.2